

# Numerical Extraction of de Haas – van Alphen Frequencies from Calculated Band Energies

P.M.C. Rourke, S.R. Julian

*Department of Physics, University of Toronto, Toronto, Ontario M5S 1A7,  
Canada*

---

## Abstract

A new algorithm for extracting de Haas – van Alphen frequencies, effective masses, and electronic density of states contributions from calculated band energies is presented. The algorithm creates an interpolated  $k$ -space “super cell”, which is broken into slices perpendicular to the desired magnetic field direction. Fermi surface orbits are located within each slice, and de Haas – van Alphen frequencies, effective masses and density of states contributions are calculated. Orbita are then matched across slices, and extremal orbits determined. This technique has been successful in locating extremal orbits not previously noticed in the complicated topology of existing  $\text{UPt}_3$  band-structure data; these new orbits agree with experimental de Haas – van Alphen measurements on this material, and solidify the case for a fully-itinerant model of  $\text{UPt}_3$ .

*Key words:* dHvA, de Haas - van Alphen, band structure, Fermi surface, electronic structure, quantum oscillations, effective mass, band mass, density of states

*PACS:* 71.15.-m, 71.15.Dx, 71.18.+y, 71.20.-b

---

## 1 Introduction

The Fermi surface of a metal is a surface of constant energy in momentum space ( $k$ -space) that, at absolute zero, separates occupied and unoccupied electron states. Determination of the Fermi surface topology of any new metallic compound is an important step toward understanding the physics of the material, since electronic properties depend sensitively on the Fermi surface shape. A powerful experimental Fermi surface probe is measurement of the quantum oscillatory magnetization, known as the de Haas – van Alphen (dHvA) effect [1].

---

*Email address:* p.rourke@utoronto.ca (P.M.C. Rourke).

At zero temperature, in the presence of a magnetic field, the free electrons of a metal undergo cyclotron motion in real space. This constrains the  $k$ -space electron states to lie on concentric tubes, called “Landau tubes”, aligned along the magnetic field direction. Only the segments of tube within the Fermi surface contain occupied states (see Fig. 1). The radius of each tube depends on the strength of the magnetic field, such that as the field is increased, the tubes get larger and successively exit the Fermi surface. As each tube leaves the surface, it rapidly depopulates, causing quantum oscillations in magnetization and other properties. The quantum oscillations are periodic in  $1/B$ , where  $B$  is the magnetic field strength, with an oscillation frequency proportional to the extremal Fermi surface cross-sectional area perpendicular to the magnetic field direction [1]:

$$F = (\hbar/2\pi e)A \quad (1)$$

where  $F$  is the dHvA frequency, and  $A$  is the extremal area. Furthermore, as temperature is increased, the Fermi surface increasingly blurs, damping out the quantum oscillations. The damping strength depends on the effective mass of the electrons averaged around the extremal orbit being measured. Thus, dHvA measurements performed as a function of temperature and magnetic field direction directly reveal both the topology of the Fermi surface and the effective electron masses on the extremal orbits of each Fermi surface sheet [1].

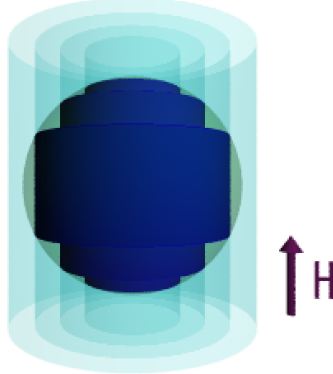


Fig. 1. Landau tubes intersecting a spherical Fermi surface. Only the sections of tube inside the Fermi surface have occupied states. In this case, only the orbit around the equator is extremal, so only one dHvA frequency would be observed.

### 1.1 Basic concepts of Fermiology (may be skipped by readers familiar with the subject)

For readers new to Fermi surface measurements, a few definitions are required. Since, at zero temperature, the Fermi surface separates occupied from unoccupied  $k$ -space states, an *orbit* refers to a path along this surface that an

electron may trace out under the influence of a magnetic field; in our case, we are dealing with orbits that not only lie on the constant-energy Fermi surface, but on a plane perpendicular to the applied magnetic field as well. A *closed orbit* is one that forms a closed loop around some part of the Fermi surface. An *extremal orbit* is a particular closed orbit whose cross-sectional area is either locally maximum or locally minimum, compared to adjacent orbits on the same Fermi surface sheet at the same magnetic field angle. Only extremal orbits are detected as quantum oscillation frequencies in a dHvA experiment; *I*, *II* and *III* in Fig. 2 are examples of extremal orbits that occur at various angles in UPt<sub>3</sub>.

The *Brillouin zone* (or equivalently, the *reciprocal unit cell*, depending on the particular volume of  $k$ -space enclosed) is the basic unit of momentum space, which repeats in all directions just as the real-space unit cell of a crystal does. As shown in Fig. 2, sometimes a Fermi surface links up with copies of itself in neighbouring Brillouin zones, forming one infinitely large, complicated shape. On such a surface, it is possible to have *open orbits*: orbits that continue forever in one direction, never coming back on themselves to form a closed loop. *IV* in Fig. 2 is an example of an open orbit. While open orbits cannot be detected in quantum oscillation measurements, their presence can be inferred from other experiments, such as angle-resolved magnetoresistance. *Near-open orbits* are closed, extremal orbits that would become open at a slightly different magnetic field angle. *III* in Fig. 2 is a near-open orbit, because a small change in magnetic field angle will transform it into an open orbit similar to *IV*. Finally, when determining the orbit type of a particular extremal orbit, an *electron orbit* is one that encloses occupied states, separating them from the unoccupied states outside the orbit; conversely, a *hole orbit* is one that encloses unoccupied states, and is associated with the motion of a “hole” through a Fermi sea of electrons rather than motion of a single electron itself.

## 1.2 Comparison to band structure

In order to understand the physical implications of dHvA data, the measured frequencies and masses are compared to those predicted by electronic structure calculations. However, since real compounds often possess complicated Fermi surfaces, including open/near-open, nested and non-central orbits, the task of extracting predicted dHvA orbits from calculated band energies is non-trivial.

One previous approach involved fitting the calculated band energies to a Fourier series of lattice-specific star functions, which was then evaluated at various points in  $k$ -space. An orbit centre and plane would be manually specified, then the algorithm would perform a series of “stepping” and “return-to-surface” operations as a function of rotation angle around the orbit centre to

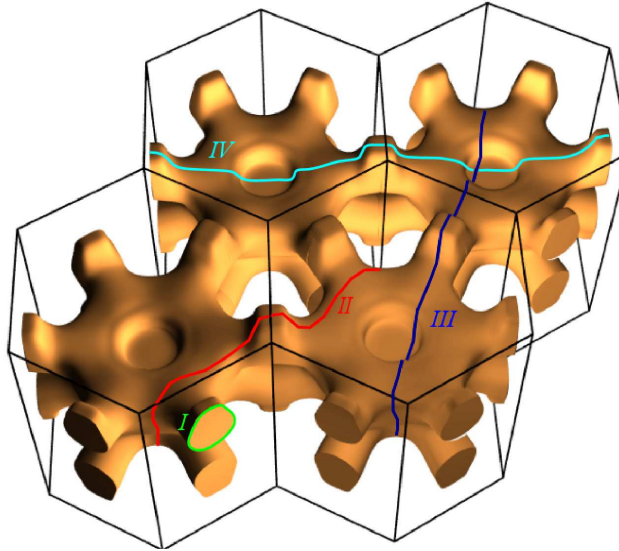


Fig. 2. The band 2 Fermi surface of  $\text{UPt}_3$ , tiled in several Brillouin zones (modified from [2]). *I* is a simple closed orbit, easily identified as extremal by visual inspection; *II* is a less-obvious extremal orbit that crosses Brillouin zone boundaries; *III* is a near-open extremal orbit; and *IV* is an open orbit.

determine the cross-sectional area via Simpson's-rule integration [3]. This approach was later expanded to include trapezoidal-rule integration for orbits which are multivalued at certain angles around the orbit centre [4]. While such an approach works well for when one knows which orbits are extremal (and the location of the associated orbit centres), topologically-complicated Fermi surfaces can have extremal orbits that are not obvious from visual examination of the surfaces.

## 2 Numerical method

### 2.1 Overview

Our algorithm is designed to exploit the large processing capabilities of current desktop computers in order to automatically extract extremal orbits, effective masses and density of states contributions from calculated Fermi surfaces of arbitrary topology, without requiring manual guidance or bias from the user. The code is written in the Fortran 90 language, and reads files defined in the XCrysDen Band-XCrysDen-Structure-File (BXSF) format. BXSF files specify band energies on a three-dimensional grid within a parallelepiped Reciprocal Unit Cell (RUC) defined by three reciprocal lattice vectors:  $\vec{a}$ ,  $\vec{b}$ , and  $\vec{c}$  [5]. Typical input files prepared for our algorithm contain on the order of 20 000  $k$ -points, whose band energies have been calculated by an electronic structure

program such as WIEN2k [6].

Upon reading the input file, the following steps are performed:

- (1) A cubic  $k$ -space Super Cell (SC), considerably larger than the original reciprocal unit cell and aligned with the desired magnetic field vector, is constructed (section 2.2). A coordinate transformation maps the super-cell  $k$ -point grid back into the reciprocal unit cell. Band energies at each of the super-cell grid points are determined from those provided in the reciprocal unit cell via Lagrange interpolating polynomials. The density of  $k$ -points in the super-cell grid is typically much greater than that of the reciprocal-unit-cell grid.
- (2) The super-cell grid is divided into slices 1  $k$ -point thick, perpendicular to the magnetic field vector. On each slice, the program scans through the  $k$ -points, locating as orbits the Fermi surface outlines (section 2.3). The cross-sectional area, effective mass and orbit type (hole or electron) are calculated for each orbit (section 2.4).
- (3) Orbit data are matched from slice to slice, so that each orbit is associated with a particular Fermi surface sheet (section 2.5).
- (4) On each Fermi surface sheet, the orbits which are extremal are singled out (section 2.6). The orbit data for similar orbits found on separate sheets are averaged, and the results output to a file.
- (5) If automatic rotation is enabled, steps 1–4 are repeated for each new magnetic field vector.
- (6) The electronic density of states contribution for the band is calculated by comparing the reciprocal-unit-cell occupied states  $k$ -space volume at energy iso-levels slightly above and below the Fermi energy to those at the actual Fermi energy (section 2.7).

## 2.2 $k$ -space super cell construction

Our algorithm operates in a large cubic  $k$ -space Super Cell (SC), which is aligned with the magnetic field direction and contains many tiled copies of the Reciprocal Unit Cell, so the first task is to construct this cell (Fig. 3) and populate it with band energies.

The reciprocal lattice vectors are defined in the BXSF file relative to  $k$ -space axes  $\hat{x}_{RUC}$ ,  $\hat{y}_{RUC}$ ,  $\hat{z}_{RUC}$ , such that, for example:

$$\vec{a} = (a_x, a_y, a_z) = a_x \hat{x}_{RUC} + a_y \hat{y}_{RUC} + a_z \hat{z}_{RUC} \quad (2)$$

According to convention, these axes are chosen so that  $\vec{a}$  lies along  $\hat{x}_{RUC}$  (that is,  $a_y = a_z = 0$ ); for a cubic or tetragonal reciprocal unit cell,  $\vec{b}$  lies along  $\hat{y}_{RUC}$

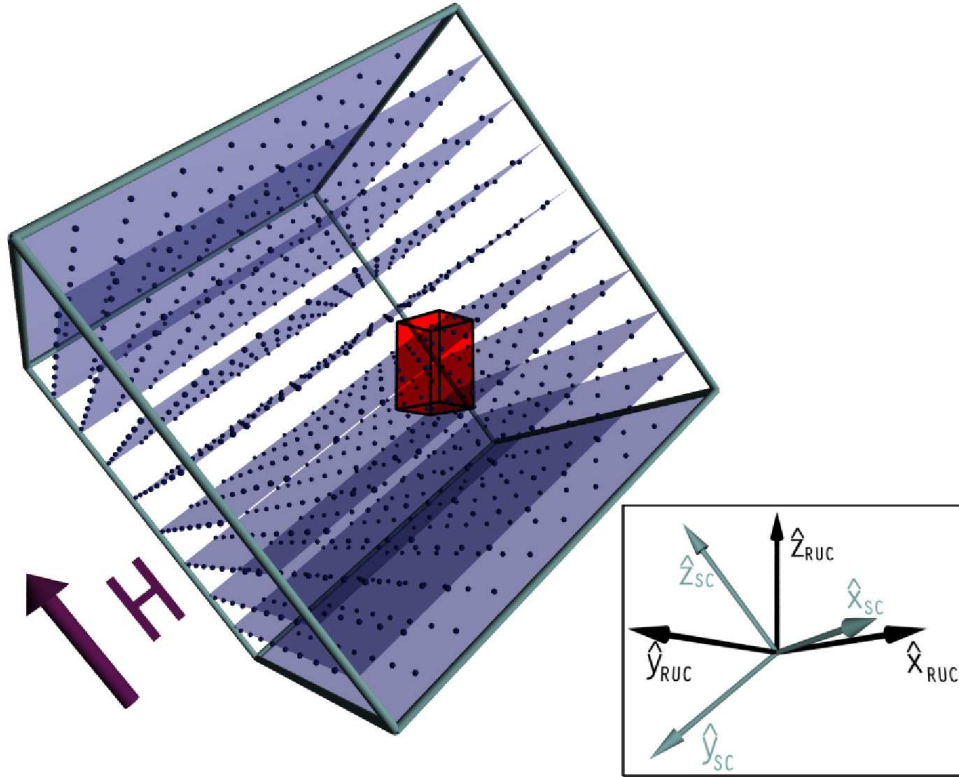


Fig. 3. An example super cell, aligned with the magnetic field  $H$ , and drawn to-scale with the small reciprocal unit cell contained within. The super cell is cut into slices perpendicular to the magnetic field, which are populated with grid points. A typical super cell would contain 600 slices, each holding  $600 \times 600$  grid points: far more than shown here. The axes for the reciprocal-unit-cell and super-cell coordinate systems are inset.

and  $\vec{c}$  lies along  $\hat{z}_{RUC}$ . Since the super cell is aligned with the magnetic field ( $\hat{z}_{SC} \parallel \vec{H}$ ), it has a different coordinate system, and a coordinate transformation is needed to map the super-cell points back to the original reference frame:

$$\begin{bmatrix} \hat{x}_{SC} \\ \hat{y}_{SC} \\ \hat{z}_{SC} \end{bmatrix} = \begin{bmatrix} v^2u + t & -vwu & -ws \\ -vwu & w^2u + t & -vs \\ ws & vs & t \end{bmatrix} \begin{bmatrix} \hat{x}_{RUC} \\ \hat{y}_{RUC} \\ \hat{z}_{RUC} \end{bmatrix} \quad (3)$$

where  $s = \sin \phi$ ,  $t = \cos \phi$ ,  $u = 1 - \cos \phi$ ,  $v = \sin \theta$ ,  $w = \cos \theta$ ,  $\phi$  is the polar angle of the magnetic field measured from  $\hat{z}_{RUC}$  down toward the  $\hat{x}_{RUC}-\hat{y}_{RUC}$  plane, and  $\theta$  is the azimuthal angle of the magnetic field measured from  $\hat{x}_{RUC}$  toward  $\hat{y}_{RUC}$ . Both coordinate systems share the same origin.

No matter what the shape of the reciprocal unit cell, the super cell is always a cube with sides defined to be 4× longer than the longest reciprocal lattice

vector. This way, for any magnetic field orientation, the super cell will contain enough tiled reciprocal unit cells to be able to track orbits which cross the zone boundaries. The super cell is situated so that 1/4 of the side length lies along  $-\hat{x}_{SC}$  while 3/4 of the side length lies along  $+\hat{x}_{SC}$ , and similarly for the other dimensions. The density of  $k$ -points in the super-cell grid is typically 100–200× greater than that of the reciprocal-unit-cell grid.

The  $k$ -points in the super cell are transformed to the reciprocal-unit-cell reference frame via Eq. 3, and translated into the volume of the original reciprocal unit cell. However, since the calculated band energies are positioned uniformly on a reciprocal-unit-cell  $k$ -point grid defined by the reciprocal lattice vectors, and these in turn are not necessarily at right angles to one another, a further transformation is necessary to allow the super-cell points to be compared to those read from the input file. A point  $\vec{p} = p_x \hat{x}_{RUC} + p_y \hat{y}_{RUC} + p_z \hat{z}_{RUC}$  maps to a point  $\vec{q} = q_a \hat{a} + q_b \hat{b} + q_c \hat{c}$  in the input array as:

$$\vec{q} = \mathbf{M}^{-1} \vec{p}, \text{ where } \mathbf{M} = \begin{bmatrix} a_x & b_x & c_x \\ a_y & b_y & c_y \\ a_z & b_z & c_z \end{bmatrix} \quad (4)$$

Once the super-cell  $k$ -points have been appropriately mapped back to the space of the input array, their band energies may be derived from those originally calculated by the electronic structure program. Since few re-mapped super-cell grid points will coincide exactly with reciprocal-unit-cell grid points, a series of third-order Lagrange interpolating polynomials [7] on a  $4 \times 4 \times 4$ -point grid are used to determine each super-cell  $k$ -point band energy.

### 2.3 Fermi surface orbit detection

Upon population with band energies, the super cell is cut into 1- $k$ -point-thick slices perpendicular to the magnetic field direction. In each super-cell slice, the program steps through the two-dimensional  $k$ -point array, locating all Fermi surface orbit outlines (details of this process are shown in Fig. 4). Fermi surface points and associated energy slopes are determined around each orbit. Orbit which run into the super cell boundaries are ignored – this limits open orbits (the super cell is large enough that copies of non-open orbits will be found elsewhere).

Note that during the “Record Fermi surface point between  $(x, y)$  and  $(x_g, y_g)$ ” algorithm step (Fig. 4), the Fermi surface point is not simply placed halfway between  $(x, y)$  and  $(x_g, y_g)$ , but rather linearly interpolated between the two

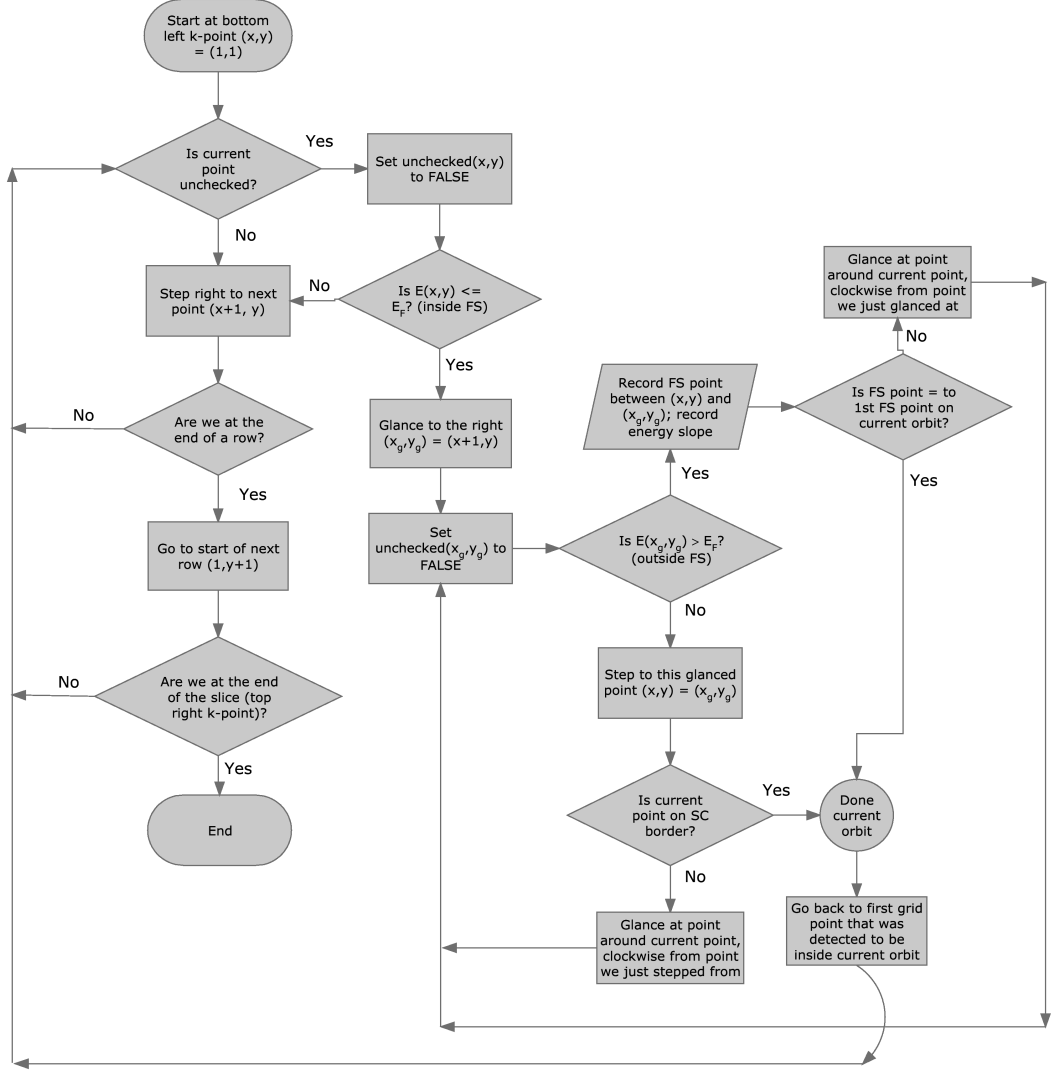


Fig. 4. Flow chart showing the Fermi surface orbit detection algorithm for finding Fermi surface outlines (orbits) within a given slice. Coordinates  $(x, y)$  refer to grid points in the two-dimensional array of  $k$ -points on the slice.

so that its position on the slice is given by:

$$x_{FS} = x + \frac{|E(x,y) - E_F|}{|E(x,y) - E_F| + |E(x_g, y_g) - E_F|} (x_g - x) \quad (5)$$

$$y_{FS} = y + \frac{|E(x,y) - E_F|}{|E(x,y) - E_F| + |E(x_g, y_g) - E_F|} (y_g - y)$$

To further clarify the core Fermi surface detection algorithm presented in Fig. 4, the action of this procedure on a small portion of an example slice is shown in Fig. 5. The algorithm has already been stepping around by the time it arrives at the depicted portion of the slice. The operations performed, in order, are:

- (1) Arrive at (2,3).  $E(2, 3)$  is not  $\leq E_F$ .

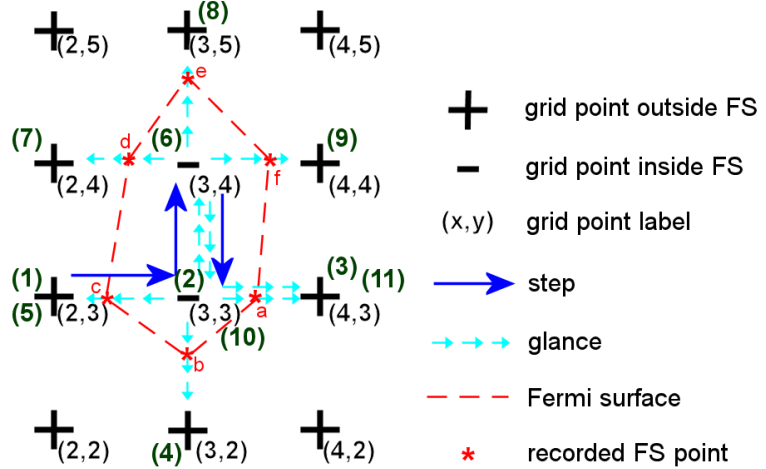


Fig. 5. Small portion of an example slice. “+” grid points have energies greater than the Fermi energy; “-” grid points have energies less than the Fermi energy. Typical slices hold  $600 \times 600$  grid points, so orbits usually contain many more points than the trivial example shown here.

- (2) Step right to the next point,  $(3,3)$ .  $E(2,3) < E_F$ .
- (3) Glance from  $(3,3)$  to the right at  $(4,3)$ .  $E(4,3) > E_F$ , so Fermi surface point  $a$  and the energy slope are recorded between  $(3,3)$  and  $(4,4)$ .
- (4) Glance around  $(3,3)$  clockwise to  $(3,2)$ .  $E(3,2) > E_F$ , so Fermi surface point  $b$  and the energy slope are recorded between  $(3,3)$  and  $(3,2)$ .
- (5) Glance around  $(3,3)$  clockwise to  $(2,3)$ .  $E(2,3) > E_F$ , so Fermi surface point  $c$  and the energy slope are recorded between  $(3,3)$  and  $(2,3)$ .
- (6) Glance around  $(3,3)$  clockwise to  $(3,4)$ .  $E(3,4)$  is not  $> E_F$ , so step from  $(3,3)$  to  $(3,4)$ .
- (7) Glance around  $(3,4)$  clockwise from  $(3,3)$  to  $(2,4)$ .  $E(2,4) > E_F$ , so Fermi surface point  $d$  and the energy slope are recorded between  $(3,4)$  and  $(2,4)$ .
- (8) Glance around  $(3,4)$  clockwise to  $(3,5)$ .  $E(3,5) > E_F$ , so Fermi surface point  $e$  and the energy slope are recorded between  $(3,4)$  and  $(3,5)$ .
- (9) Glance around  $(3,4)$  clockwise to  $(4,4)$ .  $E(4,4) > E_F$ , so Fermi surface point  $f$  and the energy slope are recorded between  $(3,4)$  and  $(4,4)$ .
- (10) Glance around  $(3,4)$  clockwise to  $(3,3)$ .  $E(3,3)$  is not  $> E_F$ , so step from  $(3,4)$  to  $(3,3)$ .
- (11) Glance around  $(3,3)$  clockwise from  $(3,4)$  to  $(4,3)$ .  $E(2,4) > E_F$ , so an Fermi surface point and the energy slope are recorded between  $(3,3)$  and  $(4,3)$ . This Fermi surface point is the same as the first one found on the orbit (Fermi surface point  $a$ , in step 3): this orbit is done!

## 2.4 dHvA frequency, effective mass, and orbit type calculations

For each orbit (i.e. Fermi surface outline) found in a particular slice, the dHvA frequency, effective mass and orbit type are calculated. Since the frequency is proportional to the cross-sectional Fermi surface area (Eq. 1), it is obtained from the area of the polygon formed by the Fermi surface points (e.g. points *a*–*f* in Fig. 5):

$$F = \frac{\hbar}{2\pi e} \left| \frac{1}{2} \sum_{i=1}^{N-1} (x_{FS,i} y_{FS,i+1} - x_{FS,i+1} y_{FS,i}) \right| \quad (6)$$

where the sum is over the points on the orbit, with the last point on the orbit same as the first:  $(x_{FS,N}, y_{FS,N}) \equiv (x_{FS,1}, y_{FS,1})$ . Note that although the “frequencies” are calculated for every orbit, cross-sectional areas only produce experimentally-measurable dHvA frequencies when they are extremal; the extremal orbits are singled out later (section 2.6).

The effective mass calculation draws upon the energy slopes at the Fermi surface. As one averages around an Fermi surface outline, two different geometric cases are encountered. If the glance directions for point *i* and point *i* + 1 are parallel (e.g. points *c* and *d* in Fig. 5), then:

$$\left| \frac{dE}{dk} \right|_i = \sqrt{\left( \frac{dE}{dk_{||}} \right)_i^2 + \left( \frac{dE}{dk_{\perp}} \right)_i^2} \quad (7)$$

where  $\left( \frac{dE}{dk_{||}} \right)_i$  is the energy slope parallel to the glance direction at point *i* (i.e. across the Fermi surface), and  $\left( \frac{dE}{dk_{\perp}} \right)_i$  is the energy slope perpendicular to the glance direction at point *i*. If the glance directions for point *i* and point *i* + 1 are perpendicular (e.g. points *a* and *b* in Fig. 5), then:

$$\left| \frac{dE}{dk} \right|_i = \sqrt{\left( \frac{dE}{dk_{||}} \right)_i^2 + \left( \frac{dE}{dk_{||}} \right)_{i+1}^2} \quad (8)$$

The effective mass averaged around the orbit, given in units of the electron mass  $m_e$ , is:

$$m^* = \frac{\hbar^2}{2\pi m_e} \left( \frac{dA}{dE} \right) = \frac{\hbar^2}{2\pi m_e} \sum_{i=1}^{N-1} \frac{\sqrt{(x_{FS,i+1} - x_{FS,i})^2 + (y_{FS,i+1} - y_{FS,i})^2}}{\left| \frac{dE}{dk} \right|_i} \quad (9)$$

Note that Eq. 9 is only correct for extremal orbits, when the energy gradient lies within the slice.

Since the orbit-finding algorithm (section 2.3) always steps around the inside of electron orbits (e.g. Fig. 5) and the outside of hole orbits, the orbit type is determined by comparing the orbit area to the area bounded by the polygon formed by the “stepped-on” grid points. If the orbit area is larger than the stepped-on area, it is flagged as an electron orbit; if the reverse is true, it is flagged as a hole orbit. At this point, average coordinates, coordinate standard deviations, maximum coordinates, and minimum coordinates for the orbit outline are also calculated.

## 2.5 Slice-to-slice orbit matching

Once the orbits outlines have been located on all slices in the super cell, Fermi surface sheets must be reconstructed by matching orbits on adjacent slices. In order for an orbit  $i$  on one slice to be matched with an orbit  $j$  on the preceding slice, and therefore added to orbit  $j$ ’s sheet, all of the following conditions must be met:

- The average  $x_{FS}$  and  $y_{FS}$  coordinates of orbit  $i$  are both within one standard deviation of the average  $x_{FS}$  and  $y_{FS}$  coordinates of orbit  $j$ .
- The maximum  $x_{FS}$  and  $y_{FS}$  coordinates of orbit  $i$  are both within two standard deviations of the maximum  $x_{FS}$  and  $y_{FS}$  coordinates of orbit  $j$ .
- The minimum  $x_{FS}$  and  $y_{FS}$  coordinates of orbit  $i$  are both within two standard deviations of the minimum  $x_{FS}$  and  $y_{FS}$  coordinates of orbit  $j$ .

If multiple orbits on one slice satisfy the conditions for matching with an orbit on the preceding slice, the parameter  $B_i$  is calculated for each candidate orbit, and the orbit with the lowest  $B_i$  value is chosen for the match:

$$B_i = \left[ \text{avg}(x_{FS})_j - \text{avg}(x_{FS})_i \right]^2 + \left[ \text{avg}(y_{FS})_j - \text{avg}(y_{FS})_i \right]^2 + \left[ \text{max}(x_{FS})_j - \text{max}(x_{FS})_i \right]^2 + \left[ \text{max}(y_{FS})_j - \text{max}(y_{FS})_i \right]^2 + \left[ \text{min}(x_{FS})_j - \text{min}(x_{FS})_i \right]^2 + \left[ \text{min}(y_{FS})_j - \text{min}(y_{FS})_i \right]^2 \quad (10)$$

## 2.6 Extremum determination

If an orbit has a frequency (cross-sectional area) which is greater than both of the adjacent orbits on the same sheet, or less than both of the adjacent orbits, it is taken to be extremal. Once all extremal orbits in the super cell have been selected, they are sorted by frequency, and those which have frequencies

within 1% of the next smallest orbit are taken to be multiple copies of the same orbit. Since the super cell contains more than one reciprocal unit cell, it is expected that multiple copies of a given extremal orbit will be found. The copies have their frequencies, effective masses and orbit types (electron = 1, hole = -1; useful for confirming that orbits of different type haven't been put on the same sheet) averaged, with standard deviations used to provide an indication of error bounds on these quantities.

## 2.7 Density of states calculation

Calculation of the band contribution to the electronic density of states proceeds separately from the super cell calculations, and is only performed once for a given input file (compared to the many repeated super-cell iterations for different magnetic field directions). To determine the density of states contribution, the following steps are executed:

- (1) The band energies within the reciprocal unit cell are interpolated very finely. No super cell is used.
- (2) The  $k$ -space volume of the reciprocal unit cell and volume per interpolated  $k$ -point are calculated.
- (3) The number of occupied points (those with  $E_{\vec{k}} < E_F$ ) are counted, and the occupied volume  $V_F$  calculated.
- (4) The number of points within an iso-surface at  $E_+ = E_F + dE$ , with typical  $dE = 0.00001 E_F$ , are counted, and the volume of such points  $V_+$  calculated.
- (5) The number of points within an iso-surface at  $E_- = E_F - dE$  are counted, and the volume of such points  $V_-$  calculated.

The electronic density of states (DOS) contributions are then:

$$DOS_{\pm} = \frac{|V_F - V_{\pm}|}{dE} \quad (11)$$

with an indication of error bounds given by the difference between + and - values.

### 3 Results

#### 3.1 Test Fermi surfaces: sphere and cylinder

In order to validate our algorithm, two artificial cases with exactly known results were constructed and used as program inputs. First, a spherical Fermi surface was generated, with band energies that depend on the square of the  $k$ -space distance from the Fermi surface centre. The input file contained band energies specified on a  $28 \times 28 \times 28$  grid in a cubic reciprocal unit cell, picked such that the effective mass  $m^* = 10.543 m_e$  and dHvA frequency  $F = 1.568$  kT, constant for all magnetic field angles. Second, a cylindrical Fermi surface was generated, with band energies that depend on the square of the  $k$ -space distance from the  $\hat{z}_{RUC}$  axis. The input file energies were specified on the same grid and reciprocal unit cell as the spherical case, and picked such that the effective mass  $m^* = 3.457 m_e$  and dHvA frequency  $F = 2.346$  kT when the magnetic field is aligned with the  $\hat{z}_{RUC}$  axis. As the field is rotated away from the  $\hat{z}_{RUC}$  axis by an angle  $\phi$ , the frequency should increase as  $1/\cos \phi$ , asymptoting to an open orbit as  $\phi \rightarrow 90$  degrees.

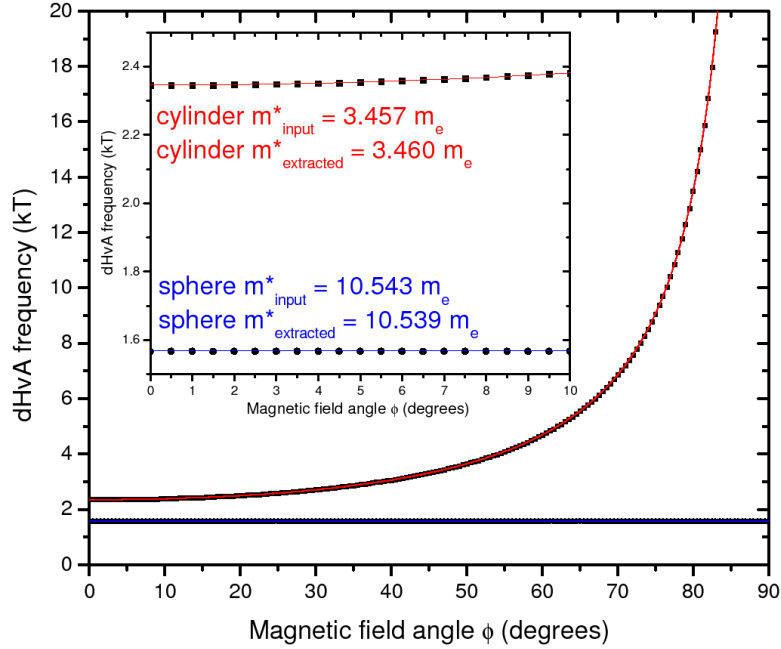


Fig. 6. de Haas – van Alphen frequency plotted as a function of magnetic field angle  $\phi$  for spherical (bottom) and cylindrical (top) test Fermi surfaces. The cylinder axis lies along the  $\phi = 0$  direction. Data extracted by our algorithm are shown as points; exact results are shown as solid lines. The inset shows a close-up of the low-angle region, as well as the exact input effective masses and corresponding band masses extracted by our algorithm for both cases.

Fig. 6 shows the results our program obtained from these two test cases. In both cases, agreement with the input values is excellent, particularly in light of the coarseness of the starting band energy grid. For the spherical case, our algorithm extracted a frequency of  $F = 1.566$  kT and mass of  $m^* = 10.539 m_e$ , varying by less than 0.002 kT and 0.002  $m_e$  respectively over the angular range tested. For the cylindrical case, with field directed along the  $\hat{z}_{RUC}$  axis, our algorithm extracted a frequency of  $F = 2.345$  kT and mass of  $m^* = 3.460 m_e$ . As the field is rotated away from the  $\hat{z}_{RUC}$  axis, the extracted frequency follows the predicted  $1/\cos\phi$  curve very closely.

### 3.2 UPt<sub>3</sub>

Having validated our computational approach, we applied it to a material of current interest: the heavy fermion superconductor UPt<sub>3</sub>, which has a hexagonal crystal structure. The term “heavy fermion” is used to describe this material, because strong electron-electron correlations lead to a very large effective mass – the conductance electrons act very “heavy”. Traditional UPt<sub>3</sub> band structure calculations, in which all uranium 5f-electrons are itinerant rather than localized, find 5 energy bands crossing the Fermi energy [8], including the complicated Fermi surface sheet shown in Fig. 2. Comprehensive quantum oscillation experiments have been performed on this compound [2], and while the orbit shapes generally agree well with band structure, some frequencies seen experimentally had no counterparts from the calculation.

By using the previously-calculated UPt<sub>3</sub> band structure information [8] as input to our program, we were able to rigorously determine the frequencies that should be seen by dHvA. Through this process, in addition to confirming the previously-known orbits, we found *new extremal orbits in the old band structure calculation* that correspond to the experimentally-measured frequencies which had until now been orphaned [2]. One such frequency, labeled  $\eta$ , corresponds to orbit *II* in Fig. 2 – since it is difficult to see by eye that this orbit is extremal, it had not been noticed prior to our work.

Full frequency versus magnetic-field-angle results for all 5  $E_F$ -crossing bands are shown in Fig. 7. Good agreement between measured and calculated Fermi-surface shape (manifested in the frequency variation with angle), but not size (manifested in the overall magnitude of the frequencies) is usual for heavy fermion materials, because their unusually flat bands mean that small shifts of the Fermi energy can produce large changes in the size of a Fermi surface sheet. Since our calculation has located previously-missing orbits in the traditional band structure data, thus bringing it into closer agreement with the experimental results, it has helped resolve a recent controversy over the fundamental itinerant nature of the UPt<sub>3</sub> 5f conduction electrons [2].

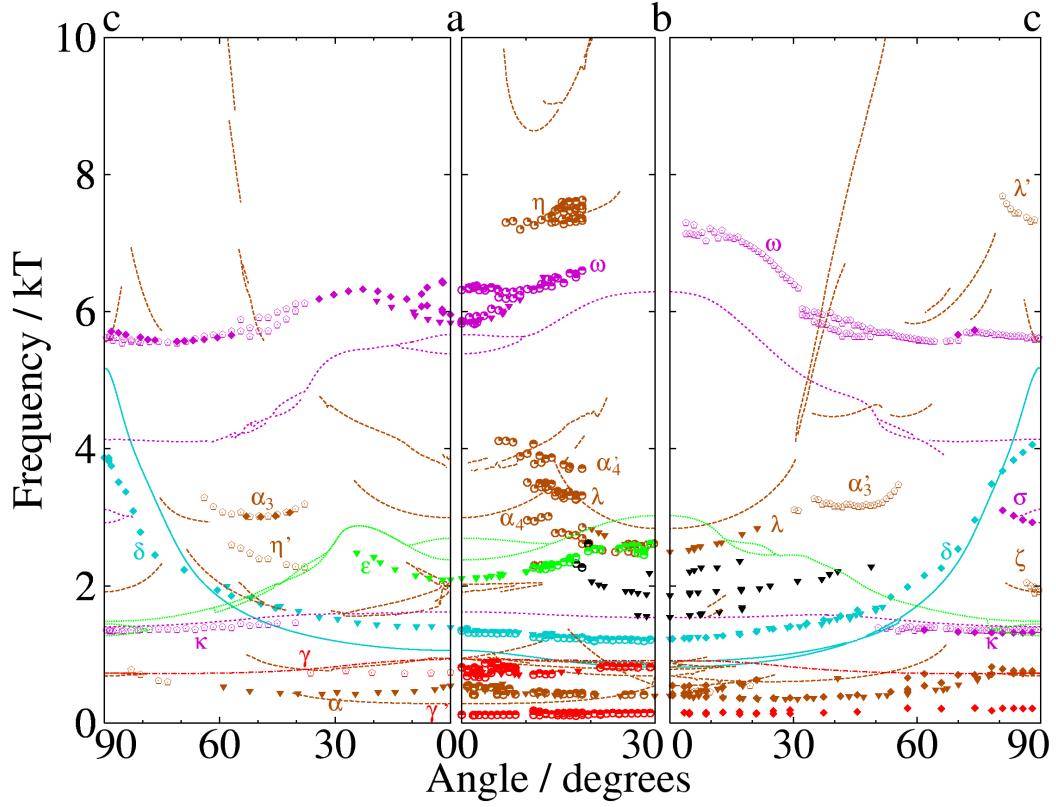


Fig. 7. Measured and calculated  $\text{UPt}_3$  de Haas – van Alphen frequencies as a function of magnetic field angle (from [2]). Solid and dotted lines are frequencies extracted from a fully-itinerant band structure calculation by our algorithm. Points are experimental measurements, with Greek letters indicating orbit labels. The  $\eta$  orbit (orbit *II* in Fig. 2) is one of the new extremal orbits found in the band structure data by our algorithm.

#### 4 Conclusion

We have developed a new approach for extracting quantum oscillation frequency, effective mass, orbit type and electronic density of states contribution from calculated band energies. By employing a large, heavily-interpolated  $k$ -space super-cell and exploiting recent advances in desktop computing power, our program can robustly characterize complicated Fermi surfaces to locate all extremal orbits.

In addition to excellent performance on simple test Fermi surfaces, when applied to the complicated energy bands of  $\text{UPt}_3$  our algorithm located new frequencies which had not been previously found on the calculated Fermi surface. These new frequencies increase the agreement between model and experiment, providing new evidence for the itinerant nature of the  $5f$  electrons in this material.

## 5 Acknowledgements

The authors would like to acknowledge useful discussions with M.R. Norman from Argonne National Laboratory. This work is supported by the Natural Science and Engineering Research Council of Canada and the Canadian Institute for Advanced Research.

## References

- [1] D. Shoenberg, Magnetic oscillations in metals, Cambridge University Press, 1984.
- [2] G.J. McMullan, P.M.C. Rourke, M.R. Norman, A.D. Huxley, N. Doiron-Leyraud, J. Flouquet, G.G. Lonzarich, A. McCollam, S.R. Julian, The Fermi surface and  $f$ -valence electron count of  $\text{UPt}_3$ , arXiv:0803.1155.
- [3] J.B. Ketterson, F.M. Mueller, L.R. Windmiller, Fourier-series representation of the Pt Fermi surface, Phys. Rev. 186 (1969) 656–666.
- [4] J.B. Ketterson, D.D. Koelling, J.C. Shaw, L.R. Windmiller, Parametrization of transition-metal Fermi-surface data, Phys. Rev. B 11 (1975) 1447–1459.
- [5] A. Kokalj, Computer graphics and graphical user interfaces as tools in simulations of matter at the atomic scale, Comp. Mat. Sci. 28 (2003) 155–168; A. Kokalj, The XSF Format Specification, available at <http://www.xcrysden.org/doc/XSF.html>.
- [6] P. Blaha, K. Schwarz, G.K.H. Madsen, D. Kvasnicka, J. Luitz, WIEN2k, An Augmented Plane Wave + Local Orbitals Program for Calculating Crystal Properties (Karlheinz Schwarz, Techn. Universität Wien, Austria), 2001. ISBN 3-9501031-1-2.
- [7] W.H. Press, S.A. Teukolsky, W.T. Vetterling, B.P. Flannery, Numerical Recipes in Fortran 77: The Art of Scientific Computing, 2nd ed., Cambridge University Press, 2001.
- [8] M.R. Norman, R.C. Albers, A.M. Boring, N.E. Christensen, Solid State Comm. 68 (1988) 245–249.